AAS 19-814

TRANSFERS FROM GTO TO SUN-EARTH LIBRATION ORBITS

Juan A. Ojeda Romero* **and Kathleen C. Howell†**

Rideshares increase launch capabilities and decrease the cost for satellite manufacturers. However, the range of orbits available for secondary payloads is dependent on launch constraints for the primary. Additionally, communications constraints and limited propellant options must be incorporated in preliminary mission design for secondary payloads. Ridesharing opportunities are now available for orbit destinations beyond LEO. In this investigation, transfers from GTOs to Sun-Earth libration point orbits are generated using stable manifold transfers and Poincaré maps.

INTRODUCTION

Rideshare launches are now more frequent as they offer opportunities to expand mission capabilities. As an example, the Lunar Crater and Observation and Sensing Satellite (LCROSS) mission was launched as a secondary payload with the Lunar Reconnaissance Orbiter (LRO) in 2009 with the objective to study hydrogen in the polar regions of the Moon.[1] This strategy decreased mission cost for LCROSS and increased the science potential for the combined venture. However, secondary payloads face several challenges, such as significantly varying orbital geometries, shifting launch dates and the impact of launch vehicle performance.[2] Shifting launch dates, in particular, are dictated by constraints on the primary payload and significantly influence the orbital geometry for the secondary payload. Additionally, secondary payloads may be further constrained due to limited on-board propulsion capabilities. Recently, propulsive EELV Secondary Payload Adapter (ESPA) rings have been proposed to increase the range of available orbits for secondary payloads. The LCROSS mission demonstrated the use of these propulsive system enhancements.[2] Some regions of interest that become available are the collinear libration points in the Sun-Earth system. The Sun-Earth L_1 libration point region is an ideal location from which to explore the solar environment while also offering favorable thermal conditions, eclipse avoidance, and continuous communications. However, preliminary transfer design must incorporate the avoidance of communications interference caused by the Sun.

Missions focused on observations of the solar environment from the L_1 region have effectively utilized quasi-periodic orbits to establish long-term orbiters. The first orbiter placed in the vicinity of the Sun-Earth L_1 collinear libration point was the successful International Sun-Earth Explorer-3 (ISEE-3), renamed the International Cometary Explorer (ICE) as the mission later evolved. The objective involved observations of the solar environment; the spacecraft successfully completed four revolutions in its Sun-Earth halo orbit before departing toward a comet via a lunar gravity assist.[3] The ISEE-3 mission was a catalyst for future long-term missions to libration point orbits. The Solar Heliospheric Observatory (SOHO) and the Advanced Composition Explorer (ACE) spacecraft were placed essentially in quasi-periodic orbits around Sun-Earth L_1[4,5] as the first dedicated missions to maintain a long-term presence in the L_1 region to observe the heliosphere and the solar wind. SOHO remains in a quasi-periodic halo orbit and ACE is currently in a Lissajous orbit around L_1. In 2004, the International Physics Laboratory (WIND) arrived near L_1 after a series of transfers through the Sun-Earth system that involved distant retrograde orbits (DROs), close approaches near L_1 and L_2, and 38 targeted lunar flybys.[6,7] The GENESIS mission involved another orbiter placed in the vicinity of

*Ph.D. Student, School of Aeronautics and Astronautics, Purdue University, Armstrong Hall of Engineering, 701 W. Stadium Ave., West Lafayette, IN 47907-2045, jojedaro@purdue.edu

†Hsu Lo Distinguished Professor of Aeronautics and Astronautics, School of Aeronautics and Astronautics, Purdue University, Armstrong Hall of Engineering, 701 W. Stadium Ave., West Lafayette, IN 47907-2045, howell@purdue.edu

L_1 with an excursion towards L_2.[8] A recent addition to the L_1 regime is the Deep Space Climate Observatory (DSCOVR), launched in 2015. The mission objectives include real-time solar wind dynamics and space weather forecasts while in a Lissajous orbit.[9,10]

Insights from Dynamical Systems Theory (DST) are frequently leveraged to investigate potential transfers to Sun-Earth libration points. While transfers are frequently constructed via numerical searches in a higher-fidelity model, fundamental understanding of the dynamical regime gained through DST in a simplified model offers efficiency and flexibility for the search effort. Periodic orbits and their invariant manifolds are frequently implemented in a search for low cost transfers.[8,11,12] Although periodic motion exists in the Circular Restricted Three Body Model (CRTBP), periodicity is not maintained when the orbit is transferred to the higher-fidelity model. In this model, quasi-periodic behavior is also available near the vicinity of the reference periodic orbit and the geometry of the final trajectory may be significantly altered as a result of the orbit selection. Thus, quasi-periodic motion near periodic orbits are viable design options to construct alternative initial guesses. Manipulating hyperbolic invariant manifolds from quasi-periodic orbits expands the search for transfers from established departure orbits.[13–15] These structures have been investigated previously in the Earth-Moon system and serve to construct transfers from locations in low Earth orbits.[16] Additionally, the existence of quasi-periodic motion is extendable for motion near irregularly shaped bodies[17] as well as formation flying.[18] Leveraging previous designs, as well as fundamental behaviors, enable trajectory options for secondary payloads.

The ridesharing scenario in this investigation involves a primary and one secondary payload. The primary payload is delivered to its geosynchronous orbit via a Geosynchronous Transfer Orbit (GTO). After launch, both payloads enter the GTO enroute to the operational geosynchronous orbit for the primary payload. After the primary payload detaches from the spacecraft, the spacecraft is comprised of a secondary payload and an auxiliary propulsive system. The orbits of interest in this investigation are the three-dimensional halo orbits in the vicinity of the Sun-Earth L_1 libration point. Additionally, at L_1, there is a communications constraint to be incorporated in preliminary mission design. In addition to launch constraints, this additional requirement bounds the range of orbits available for the secondary payload.

In this analysis, periodic and quasi-periodic motion is leveraged to construct transfers to the Sun-Earth L_1 collinear libration point from a GTO. A methodology that employs structures from halo and quasi-halo orbits is developed to examine the geometry of L_1 transfers with low maneuver magnitudes along with the orientation for a GTO. A candidate halo orbit that satisfies a set of constraints is first identified from an L_1 halo orbit family. Next, a family of quasi-halo orbits that evolves from the candidate halo orbit is constructed using a numerical process. Then, a candidate quasi-halo orbit that satisfies the constraints is selected. Potential transfers are identified on a Poincaré map that displays potential connections from quasi-halo stable manifold trajectories and departure locations along a GTO. Finally, an end-to-end trajectory is constructed by using a multiple-shooting scheme and the selected transfer from the map.

BACKGROUND

From a number of options, motion within the CRTBP can be categorized into four types: equilibrium points, periodic solutions, quasi-periodic solutions, and chaos.[19] In this investigation, emphasis is focused on quasi-periodic motion in the vicinity of an equilibrium point in the Sun-Earth CRTBP. The existence of quasi-periodic tori that emanate from periodic orbits is explored. The computation of quasi-periodic orbits and their dynamical structures is formulated for application to transfer design.

Dynamical Model

Dynamical structures in the CRTBP are frequently leveraged to produce preliminary mission design trajectories. The CRTBP[20] model describes the motion of a spacecraft, P_3, of negligible mass and subject to the gravitational force of two larger bodies, P_1 and P_2. The primary bodies, P_1 and P_2, with masses m_1 and m_2, are assumed to be in a circular orbit about their system barycenter. The rotational reference frame in the CRTBP includes an origin, O, at the barycenter of P_1-P_2. The basis vectors ($\hat{x}$,$\hat{y}$,$\hat{z}$) are defined such that the unit vector $\hat{x}$ is directed from P_1 towards P_2, $\hat{z}$ in the direction of the angular momentum vector for the

P_1-P_2 orbit, and $\hat{y}$ completes the dextral orthonormal triad. A characteristic mass parameter, $\mu = \frac{m_2}{m_1+m_2}$, is introduced as the ratio of the smaller m_2 to the total mass of the system. The system is non-dimensionalized with a characteristic length, l^*, defined as the constant distance between P_1-P_2 and a characteristic time, t^*, evaluated to render the non-dimensional mean motion of the primaries equal to unity. The non-dimensional position and rotating velocity of the spacecraft are defined such that $\bar{R} = [x, y, z]^T$ and $\bar{V} = [\dot{x}, \dot{y}, \dot{z}]^T$, respectively, where overbars reflect vectors and the superscript, ^{T}, indicates a matrix transpose. The non-dimensional position of the primaries P_1 and P_2 are fixed at $\bar{R}_1 = [-\mu, 0, 0]^T$ and $\bar{R}_2 = [1-\mu, 0, 0]^T$, respectively. The six-dimensional state of the spacecraft is defined as $\bar{X} = [x, y, z, \dot{x}, \dot{y}, \dot{z}]^T$. The non-dimensional scalar equations of motion for the system are written,

$$\ddot{x} - 2\dot{y} = \frac{\partial U^*}{\partial x} \qquad \ddot{y} + 2\dot{x} = \frac{\partial U^*}{\partial y} \qquad \ddot{z} = \frac{\partial U^*}{\partial z} \tag{1}$$

A pseudo-potential function is defined as $U^* = \frac{1-\mu}{R_{13}} + \frac{\mu}{R_{23}} + \frac{1}{2}(\dot{x} + \dot{y})$ and the distances between P_1-P_3 and P_2-P_3 are evaluated as $R_{13} = \sqrt{(x+\mu)^2 + y^2 + z^2}$ and $R_{23} = \sqrt{(x-1+\mu)^2 + y^2 + z^2}$, respectively. An integral of the motion, Jacobi Constant, exists and is evaluated as $C = 2U^* - V^2$, where $V = \sqrt{\dot{x}^2 + \dot{y}^2 + \dot{z}^2}$ is the rotating speed of the spacecraft. Five equilibrium solutions (libration points) exist in the x-y plane in this formulation. Three collinear libration points lie along the $\hat{x}$ direction and two triangular libration points lie on vertices of an equilateral triangle created with $\bar{R}_1$ and $\bar{R}_2$. The triangular points are reflected across the $\hat{x}$ axis.

Periodic Orbits

Preliminary transfer design to the Sun-Earth libration point region has previously leveraged periodic orbits and invariant manifolds to identify potential transfers and destinations. Families of periodic planar Lyapunov and out-of-plane vertical orbits emanate from the collinear points. As the planar Lyapunov orbit family evolves with respect to C, a family of out-of-plane halo orbits bifurcate from the planar family. The halo orbit family evolves in two opposite out-of-plane directions denoted northern and southern families. A family of northern L_1 halo orbits for a specified range of C is plotted in Figure 1. A southern family of periodic halo orbits also exists in this same range of Jacobi Constant values and is a reflection of the northern family across the x-y plane. Higher energy orbits are notably larger with lower C values. The family depicted in Figure 1 is not a complete representation and continuous beyond this region.

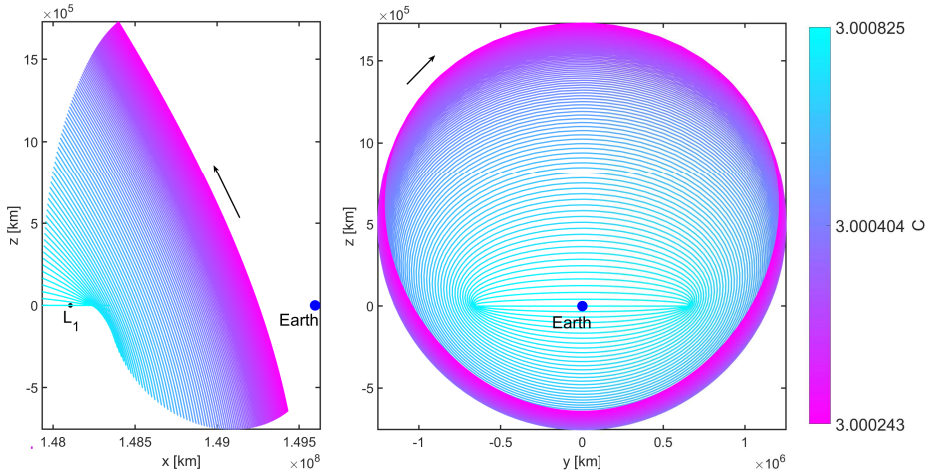

Figure 1: Family of northern halo orbits in the Sun-Earth system as modeled in the CRTBP. Higher energy orbits correspond to lower Jacobi Constant, C, values.

Surfaces of section and maps are powerful tools for analyzing complex behavior in dynamical systems. In this analysis, insights from stroboscopic and Poincaré maps are exploited. A stroboscopic map offers a snapshot of a trajectory by evolving the initial state, $\bar{X}_0$, to discrete time intervals. The State Transition

Matrix (STM), $\Phi(t, t_0)$, is a linear stroboscopic map that relates an initial state variation, $\delta\bar{X}(t_0)$, to a final downstream state variation, $\delta\bar{X}(t)$. The Poincaré map displays the return of a trajectory to a surface of section and converts a continuous time system to a discrete system.[21] Additionally, by leveraging a Poincaré map, the dimensionality of the system is reduced. A periodic orbit on a Poincaré map appears as a single point, $\bar{X}^*$, that is, a fixed point. Linear stability analysis offers insight on behavior in the vicinity of this fixed point and leverages the monodromy matrix, defined as the STM, $\Phi(T, 0)$, after precisely one orbital period, T. The eigenvalues of the monodromy matrix, λ_i, then reveal the stability characteristics of the periodic orbit. For the invariant time system in the CRTBP, the eigenvalues for the monodromy matrix occur in reciprocal pairs.[22] Given a reference periodic orbit, a pair of eigenvalues equal to unity indicates the existence of a family of periodic orbits. The remaining pairs of eigenvalues identify the characteristics of the flow near $\bar{X}^*$. Real eigenvalues with $|\lambda_i| < 1$ suggests the existence of a stable manifold; complementary real eigenvalues with $|\lambda_i| > 1$ depict the unstable manifold. Complex eigenvalues with $|\lambda_i| = 1$ are on the unit circle and reflect the existence of a center manifold. Trajectories within the global representations of these manifolds via the eigenvectors $\bar{v}_i$, are frequently analyzed to construct low cost transfers. Quasi-periodic orbits that evolve from a periodic orbit exist in the center subspace.

Quasi-Periodic Orbits

Families of quasi-periodic orbits evolve from periodic orbits and possess dynamical structures to be leveraged for transfers. While transfers can be constructed with initial guesses built on periodic orbits and their associated manifolds, families of quasi-periodic orbits may offer better design alternatives due to the bounded behavior and varying geometry. Quasi-periodic orbits exist in the center subspace (that includes periodic orbits) as invariant tori with incommensurate frequencies, ω_i. For a two-dimensional torus, illustrated in Figure 2(a), the frequencies ω_1 and ω_2 render an irrational ratio, $\frac{\omega_1}{\omega_2}$. Rational frequency ratios on a two-dimensional torus deliver a periodic orbit. As observed in Figure 2(a), any state along the red trajectory can be defined in terms of the angles θ_1 and θ_2 associated with the frequencies ω_1 and ω_2, respectively. A Poincaré map with surface of section, Σ, constructed to display multiple returns of a state defined as $\bar{u}(\theta_1, \theta_2)$, a six-dimensional state with respect to a periodic orbit fixed point, $\bar{X}^*$, as illustrated in Figure 2(b). The torus state is parametrized with the angles $\theta_i = \frac{2\pi t}{T_i}$, where T_i is the period for the corresponding frequency.[23] The returns of the trajectory form a closed curve over infinite time and the motion of a quasi-periodic orbit is bounded by the torus, a periodic orbit incurs multiple returns to a single point. In this investigation, quasi-periodic orbits associated with periodic halo orbits are computed from a set of two-dimensional tori in the Sun-Earth CRTBP system.

Computation of a Quasi-Periodic Orbit Quasi-periodic orbits are computed using an approach that relies on numerical techniques to determine a two-dimensional torus. This method originates with Gómez and Mondelo and includes enhancements by Olikara and Scheeres.[23,24] The approach is demonstrated for, but not limited to, two-dimensional tori in generating families of quasi-periodic orbits in the CRTBP. The methodology is also extended to construct quasi-periodic motion in non-autonomous systems with periodic forcing such as the Elliptic Three Body Problem (ETBP) and the Bicircular Four Body Problem (BCFBP).[13]

To numerically produce a quasi-periodic orbit, the foundation of this analysis is a periodic halo orbit represented in terms of a fixed point, $\bar{X}^*$. A stroboscopic map over time T_1 is generated to reduce the dimensionality in a search for an invariant curve. With a periodic time T_1, corresponding to the angle $\theta_1(0) = \theta_1(T_1)$, the initial and final torus states are defined on a two-dimensional torus and relative to $\bar{X}^*$ at the section as $\bar{u}\Big(\theta_1(0), \theta_2(0)\Big)$ and $\bar{u}\Big(\theta_1(T_1), \theta_2(\frac{2\pi T_1}{T_2})\Big)$, respectively. The invariant curve is parametrized by θ_2 as illustrated in Figure 2(b). For a given T_1, the final angle θ_2 is also defined as $\theta_2(\frac{2\pi T_1}{T_2}) = \theta_2(0) + \rho$, where ρ is an angle along the invariant curve, termed the rotation angle. On the first return to the map, a point $\bar{u}(\theta_1, \theta_2)$ is rotated by the angle, ρ, on the invariant curve. The search for this invariant curve is mathematically described by an invariance condition, such that the $R[-\rho]$ is a rotation matrix that rotates the final state on the torus back to its initial state, i.e.,

$$R\big[-\rho\big]\big[\bar{u}(2\pi, \theta_2(0) + \rho)\big] - \big[\bar{u}(0, \theta_2(0))\big] = \bar{0} \tag{2}$$

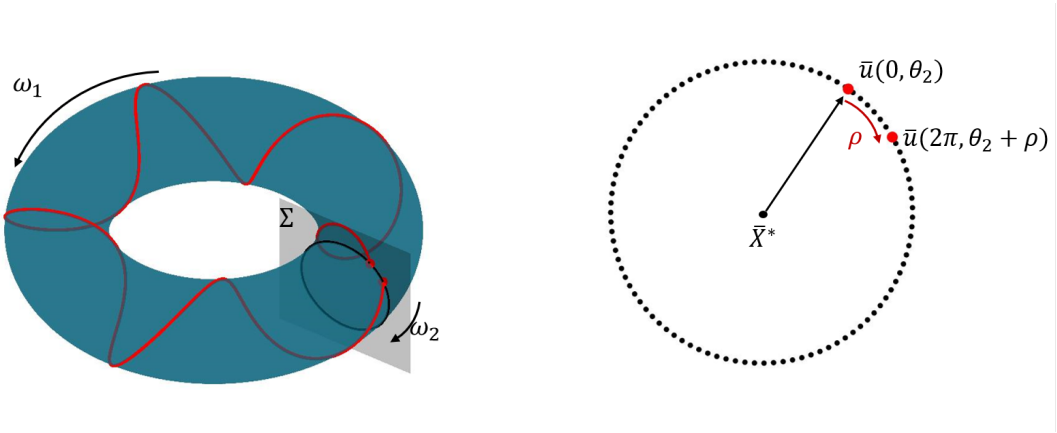

(a) (b)

Figure 2: (a) Two-dimensional torus parameterized by its fundamental frequencies. A Poincaré map with surface of section, Σ is plotted and the first return to the map is plotted in red. (b) Stroboscopic map with multiple returns from a trajectory on a torus.

In this form, the invariant curve is discretized into n torus states $\bar{u}_j$ with $j = [1, ..., n]$ by using a truncated Fourier series. In Equation (2), the torus states are row vectors and the rotation matrix is a $n \times n$ real matrix evaluated with elements of the Fourier series and the rotation angle $(-\rho)$.[24]

A multiple shooting strategy is implemented in this scheme to address the sensitivities of the trajectories in the CRTBP and deliver a quasi-periodic trajectory as a series of state vectors.[24] The propagated states along the invariant curve, $\bar{u}_j$, are subdivided into p segments, each with time $\frac{T_1}{p}$. The initial torus state for each segment is defined as $\bar{u}_j^k$, where $k = [1, ..., p]$. Equation (2) is evaluated with initial states $\bar{u}(0)_j^1$ and the final propagated states $\bar{u}(\frac{T_1}{p})_j^p$. Full state continuity is enforced for the remaining $p-1$ segments. Additionally, constraints for energy C, rotation angle ρ, or mapping time T_1 are introduced to the corrections process to evaluate an initial quasi-periodic solution. States along the invariant curve are initialized with the components of six-dimensional eigenvector, $\bar{v}_c$, in the center subspace of the reference periodic orbit. States, $\bar{u}_j$, along the invariant curve are evaluated as follows,

$$\bar{u}_j = \epsilon \left[\mathbf{Re}[\bar{v}_c] \cos\left(\frac{2\pi(j-1)}{n}\right) - \mathbf{Im}[\bar{v}_c] \sin\left(\frac{2\pi(j-1)}{n}\right) \right] \tag{3}$$

The displacement, ϵ, is evaluated with respect to a periodic fixed point associated with $\bar{v}_c$. The initial rotation angle, ρ_0, is evaluated with the angle of the eigenvalue associated with the periodic orbit in the center subspace, $\rho_0 = \mathbf{Re}[-i \log(\lambda_c)]$, where $i = \sqrt{-1}$. The stroboscopic map time T_1 is initialized as the period of the reference periodic orbit, T.

Families of quasi-periodic orbits are generated with constant values of C, rotation angle, or mapping time.[13,16] In this investigation, constant C families are produced. A multiple-shooting strategy with a pseudo-arclength continuation method is implemented to produce a family of quasi-periodic orbits. The truncated Fourier series that parametrizes the invariant curve is not unique, therefore, phasing constraints are included to prevent the corrections process from converging along the initial quasi-periodic solution.[13] For constant C families, the corrections process may suffer with convergence difficulties near large resonances. Recall that the rational frequency ratios, $\frac{\omega_1}{\omega_2}$ or $\frac{2\pi}{\rho}$, indicate the existence of periodic orbits. Near the vicinity of these rational frequencies, regions of large resonance may exist that challenge the convergence of the multiple-shooting algorithm.

Stability of Quasi-Periodic Orbits The methodology to assess the linear stability of a quasi-periodic orbit is similar to that of periodic orbits. Recall that, for periodic orbits, a linearized stroboscopic map, the mon-

odromy matrix, is leveraged to investigate the stability properties near a fixed point. No fixed points exist for quasi-periodic orbits, but stability properties emerge via the linearized stroboscopic map for the invariant curve, i.e.,

$$DP = \Big(R\big[-\rho\big] \otimes I\Big)\overline{\Phi} \tag{4}$$

The linearized stroboscopic map is represented by the matrix DP in Equation (4), where $\overline{\Phi}$ is the matrix, of size $6n \times 6n$, that includes the STM, $\Phi_j(T_1, 0)$, that incorporates the points $\bar{u}_j$ along the invariant curve, $\otimes$ is the kronecker product, and I is a 6×6 identity matrix. The eigenstructure of matrix DP is analyzed to determine the stability properties. The eigenvalues, Λ, of the linearized map occur in concentric circles.[24] The stable and unstable manifolds are characterized by evaluating if $\|\Lambda\| < 1$ and $\|\Lambda\| > 1$, respectively; they then exist as concentric circles with magnitudes that are not unity. Additionally, stability for quasi-periodic orbits are also characterized with a stability index, that is, $\nu = \frac{1}{2}\big(\frac{1}{\|\Lambda_s\|} + \|\Lambda_u\|\big)$, where values of ν close to unity are considered stable and values greater than unity are unstable.[16]

Invariant Manifolds for the Quasi-Periodic Orbit Hyperbolic invariant manifolds evolve from unstable quasi-periodic orbits and are frequently leveraged for low cost transfers. Unstable quasi-periodic orbits possess stable and unstable manifold structures that asymptotically approach and depart the quasi-periodic trajectory. In this investigation, only stable manifolds are explored to create transfers that flow towards quasi-periodic orbits. A global representation of the stable manifold emanating from the quasi-periodic orbit in reverse time leverages the real eigenvector $\bar{\Psi}_s$ which is associated with a real eigenvalue Λ_s. The eigenvector is defined with a set of column eigenvectors $\{\bar{\psi}_j^S\}$ that correspond to $\bar{u}_j$ along the invariant curve. From a point $\bar{u}_j$ on the invariant curve, a state on the stable manifold, $\bar{u}_j^S$, is approximated as follows,

$$\bar{u}_j^S = \bar{u}_j \pm d\frac{\bar{\psi}_j^S}{\|\bar{\psi}_{rj}^S\|} \tag{5}$$

In Equation (5), $\bar{\psi}_j^S$ is defined as the associated six-dimensional stable eigenvector for $\bar{u}_j$ and d is a scalar stepoff distance. Additionally, $\bar{\psi}_j^S = [\bar{\psi}_{rj}^S, \bar{\psi}_{vj}^S]^T$, where $\bar{\psi}_{rj}^S$ and $\bar{\psi}_{vj}^S$ are three-dimensional vectors such that $\bar{\psi}_{rj}^S$ corresponds to the elements associated with position and $\bar{\psi}_{vj}^S$ isolate the velocity elements. The eigenvectors along the full torus are evaluated from the STM, $\Phi(T_1, 0)$.[24]

Characterizing quasi-periodic orbits Comparisons along a family of quasi-periodic orbits is facilitated via a set of characterizing metrics. Metrics based on geometry, fundamental frequencies, ω_1 and ω_2, and C are frequently implemented for characterization along a quasi-periodic family.[23,25] In this investigation, 'box dimension' metrics are utilized to compare quasi-periodic orbits. Box dimensions for the quasi-periodic orbit X_B, Y_B , Z_B are measured along the $\hat{x}$, $\hat{y}$, and $\hat{z}$ axes, respectively, in the rotating frame. Box dimensions are not equal to maximum amplitudes in any direction and are evaluated as the difference between the maximum excursions of an orbit along an axis. For example, Y_B is evaluated as the difference between a maximum y and minimum y along the $\hat{y}$ axis for the quasi-halo orbit in Figure 3.

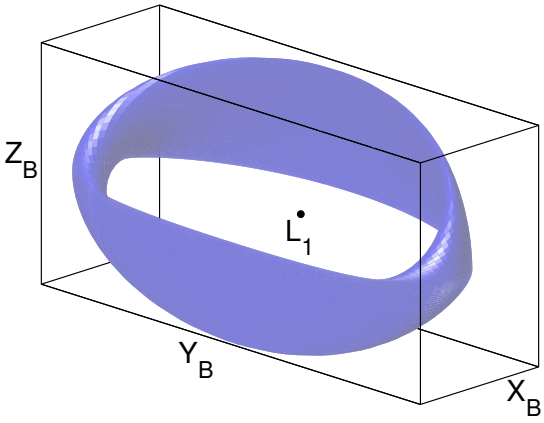

Figure 3: Box dimensions for quasi-halo orbit with $C = 3.000802$

Keplerian Orbits in CRTBP

In this investigation, a secondary payload departs from a GTO as observed in the CRTBP. These are highly eccentric Hohmann transfer orbits that frequently deliver various spacecraft to circular geosynchronous orbits

at an altitude of 35,622 km. The transfer orbit includes an apogee altitude equal to the geosynchronous orbit altitude while the perigee altitude is dependent on the performance and size of the launch vehicle and may vary from 300-1200 km. Additionally, the geometry of a GTO varies across launch windows and launch vehicle performance metrics. A GTO, computed as a Keplerian elliptical orbit, is plotted in the rotating reference frame of the CRTBP in Figure 4. In the rotating frame, the GTO is not a closed periodic orbit and its line of apsides shifts as demonstrated in Figure 4. A precession angle γ is defined to depict the shift in

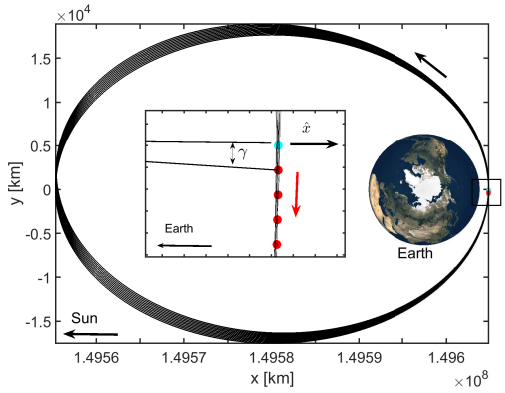

Figure 4: Geometry of GTO in the rotating frame of the CRTBP. Precession angle, γ, demonstrates the shift of the line of apsides after ten revolutions around the Earth. The direction of γ is opposite of the motion of the orbit.

the GTO perigee (i.e., the shift in the line of apsides) after a number of revolutions in the CRTBP. The angle γ is evaluated as the angle measured from the $\hat{x}$ axis and GTO perigee direction, defined with respect to the Earth. As an example, the precession angle for the GTO after one revolution in Figure 4 is $\gamma = 0.44°$. Note that the line of apsides rotates counter-clockwise and opposite to the motion of the spacecraft. The perigee is defined with $\bar{q}\dot{\bar{q}}^T = 0$ with the condition that $V^2 + \bar{q}\ddot{\bar{q}}^T \geq 0$, where $\bar{V}$ is the velocity in the rotating frame, $\bar{q} = \bar{R} - [1-\mu, 0, 0]$ is the radial distance from the Earth, $\dot{\bar{q}} = \bar{V}$, and $\ddot{\bar{q}} = [\ddot{x}, \ddot{y}, \ddot{z}]^T$. The Keplerian GTO as observed in Figure 4 possesses a perigee altitude of 1000 km and serves as the baseline geometry for this investigation. The orientation in Figure 4, defined as the midnight orientation, includes the initial perigee on $\hat{x}$ opposite side the Sun and Earth directions. The midnight orientation serves as the reference orientation for this analysis.

DESIGNING TRANSFERS

Maps are employed to construct direct transfers to quasi-periodic orbits from a set of GTO orientations. This investigation focuses on direct transfers defined as trajectories with no revolutions around the Earth, both direct and indirect transfers are compared in Figure 5. In certain scenarios, indirect transfers are targeted

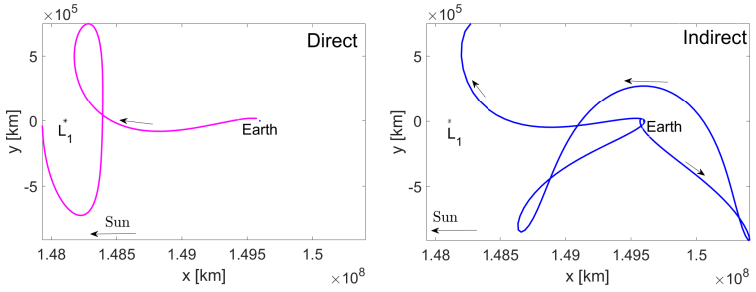

Figure 5: Direct and Indirect transfers to a quasi-periodic orbit.

as part of a tour through a system. However, direct transfers have lower times-of-flight and may avoid Earth eclipsing issues during a transfer.

Communications constraints during the Earth-to-L_1 transfer and in the Sun-Earth L_1 libration point orbit require that the spacecraft avoid crossing in front of the solar disk when viewed from the Earth.[4] In the rotating frame, a Sun-Earth-Vehicle (SEV) angle α is defined as the angle between $\bar{R}_{23}$ and -$\hat{x}$ as illustrated in Figure 6. The Solar Exclusion Zone (SEZ) is a region defined by a right circular cone with the vertex at the Earth and a constant SEV angle, i.e., $\alpha_{SEZ} = 5^\circ$ in this investigation. A function that mathematically defines crossings into the SEZ cone along a trajectory is expressed,

$$F_\alpha = \int |\sin(\alpha(t) - \alpha_{SEZ})| - \sin(\alpha(t) - \alpha_{SEZ}) dt \tag{6}$$

In this formulation, $\alpha = \tan^{-1}\{-\frac{\sqrt{y^2+z^2}}{x-1+mu}\}$ and $|\cdot|$ implies an absolute value. To prevent interference during downlink transmissions due to solar radio frequencies, transfers and any L_1 trajectories must avoid crossing into the SEZ.[4]

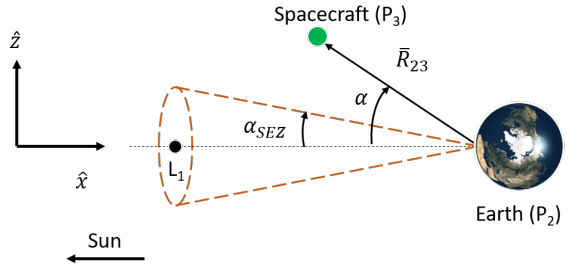

Figure 6: Solar Exclusion Zone defined in the Sun-Earth rotating frame (red). The angle α_{SEZ} is used to define the size of this region.

A multiple-shooting strategy that incorporates Newton's method for updates in a differential corrections scheme is leveraged to construct feasible solutions.[26] For constrained transfers, the function $F_\alpha = 0$ is included as an added constraint in the corrections process. In this investigation, a reference trajectory is defined as the superposition of trajectory arcs selected from a map and a specified number of revolutions of a quasi-periodic orbit. Reference trajectories are introduced with state discontinuities and input as initial guesses for the differential corrections process to produce a continuous solution with similar characteristics. The reference trajectory is constructed with three sections: a GTO arc, a stable manifold arc, and a quasi-periodic arc. The GTO arc is a propagated trajectory from the GTO perigee to a departure location. The perigee state is fixed to constrain departures from a single GTO specified orientation. The manifold arc, associated with a quasi-periodic L_1 orbit, is a trajectory selected from a crossing identified in a map and propagated forward in time. The quasi-periodic arc is generated by stacking a number of revolutions along the quasi-periodic orbit. The multiple-shooting strategy is implemented by decomposing each transfer segment along the reference solution into a series of N nodes, $\bar{X}_i = [x_i, y_i, z_i, \dot{x}_i, \dot{y}_i, \dot{z}_i, \tau_i]^T$, with $i = [0, ..., N]$.[27] All nodes are defined in terms of a full state and an arc time, τ_i. The final solution possesses full state continuity except for a velocity discontinuity at the departure location. Additionally, the final solution does not violate the SEZ constraint.

The methodology in this investigation leverages information from periodic halo orbits to build quasi-halo orbits and invariant manifold trajectories. Trajectories within the stable manifold of halo orbits pass near the Earth, but they don't necessarily pass near GTOs. However, stable manifold trajectories from quasi-halo orbits are obsrved to pass near GTOs. Maps reflect the departure locations along a GTO and appropriate stable manifold trajectories of quasi-halo orbits to construct transfer arcs for reference trajectories. The following steps are consistent in developing feasible reference trajectories:

1. Generate a GTO trajectory in Sun-Earth CRTBP. A candidate 'GTO initiating state' along the GTO

is propagated in the Sun-Earth CRTBP and observed in the rotating frame. The changing precession angle facilitates the exploration of different geometries during long intervals on the GTO.

2. Identify a candidate halo orbit that satisfies communications requirements, i.e., avoids the SEZ. The candidate orbit must possess a four-dimensional central manifold to construct two-dimensional quasi-periodic orbits.

3. Generate a family of quasi-halo orbits from the candidate halo orbit. In this investigation, only constant C families are generated. However, constant ρ and constant mapping time, T_1, families represent alternative options and are constructed similarly.[16]

4. Identify a candidate quasi-halo orbit that avoids the SEZ. The quasi-halo orbit is bounded inside an invariant surface that must be situated outside the SEZ. However, it is not necessary for the invariant surface to be entirely outside the SEZ to construct viable transfers. This scenario is not investigated here as it requires stationkeeping maneuvers to prevent crossing into the SEZ. However, this scenario is expected to occur when transitioning to a higher-fidelity model.

5. Generate trajectories within the hyperbolic stable manifold of a candidate unstable quasi-halo orbit. In this investigation, trajectories inside the stable manifold that exist close to the Earth are employed to identify direct transfers.

6. Create maps with trajectories from the stable manifold and departure locations along the GTO. Velocity magnitudes and directions are also available on the map.

7. Construct a reference trajectory from the selected arcs on the map. Correct a feasible reference trajectory to construct a viable transfer that avoids crossing into SEZ. Additional constraints, such as maximum α, are not included as part of the science requirement at this time.

The methodology in this investigation focuses on one maneuver ΔV from a departure location along a GTO and no stationkeeping maneuvers. For a given GTO, steps 2-7 may be repeated to find a variety of solutions.

A final corrected transfer possesses a ΔV magnitude which is compared to a theoretical minimum maneuver magnitude, ΔV_{min}. The ΔV_{min} is computed as,

$$\Delta V_{min} = \sqrt{2U^*_{dep} - C_{arr}} - V_{dep} \tag{7}$$

This formulation uses the Jacobi Constant difference between the departure orbit and the arrival orbit. The pseudo-potential, U^*_{dep}, and the velocity, V_{dep}, are defined at the departure location along the GTO and the Jacobi Constant for the arrival orbit is C_{arr}. Of course, the theoretical minimum is a function of the departure location along the GTO. For a fixed C_{arr}, ΔV_{min} will vary as the departure location varies along the GTO. The theoretical minimum is a metric that offers a lower bound on ΔV that is dependent on the Jacobi Constant change between the departure and arrival orbits.

CONSTRAINED TRANSFERS TO QUASI-PERIODIC ORBITS IN THE L_1 REGION

Poincaré maps are leveraged to identify connections between manifold trajectories and departure locations along a planar GTO. All potential departure locations along a planar GTO are explored with an x-y Poincaré map. The candidate GTO is defined with the following Keplerian orbital elements: semi-major axis equal to 24689.85 km, eccentricity of 0.701, and a 0° inclination with respect to the Sun-Earth ecliptic plane. The orbit propagated in the CRTBP for one Keplerian orbital period of 10.7 hr is plotted in Figure 7.

Families of periodic halo orbits and quasi-halo trajectories are constructed to identify feasible orbits near L_1. A family of northern halo orbits in the Sun-Earth L_1 vicinity is generated in Figure 8(a). The halo family continues beyond this region, but only orbits close to the L_1 libration point are included. Only a subset of the family satisfies the SEZ constraint, as apparent in Figure 8(b). A candidate halo orbit with a period equal to $T = 177.7$ days, indicated by a black line in Figure 8, is selected from this collection of orbits. The candidate

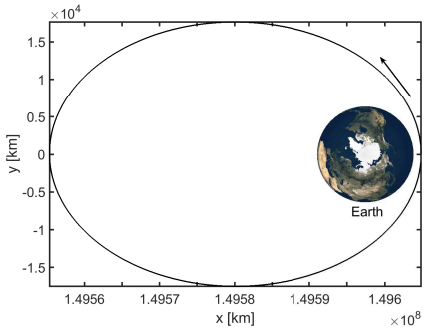

Figure 7: Initial planar GTO in the Sun-Earth rotating frame. An initial two-body state is propagated in the Sun-Earth CRTBP.

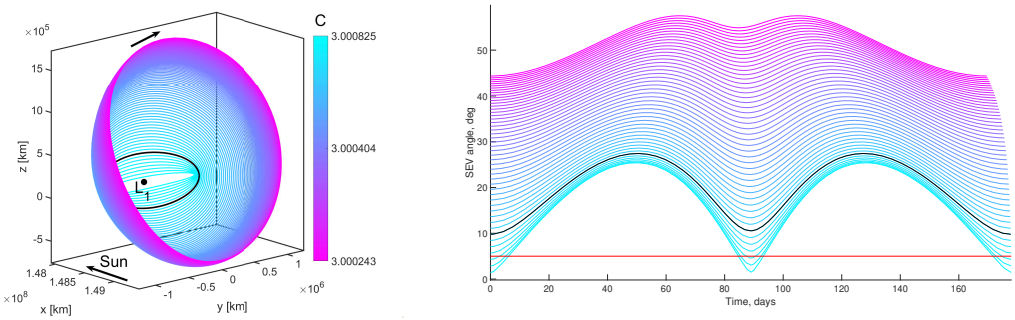

(a) (b)

Figure 8: (a) Northern halo family around Sun-Earth L_1 with a candidate halo orbit in black. (b) SEV angle, α, during one period for the northern halo family in (a).

halo orbit possesses a four-dimensional center manifold that indicates the existence of quasi-halo orbits. A family of quasi-halo orbits with a Jacobi constant equal to 3.000802 is generated near the candidate halo orbit. A sample set of quasi-halo orbits is plotted in Figure 9. The complete family is not in the figure and only a range of quasi-halo orbits remains above the SEZ constraint as demonstrated in Figure 9. The candidate quasi-halo orbit is unstable and corresponds to $\rho = 0.19358$ rad in Figure 9 and does not violate the SEZ. The eigenvector, $\bar{\Psi}_S$, reflecting the stable manifold, is identified and the trajectories along the manifold are propagated in reverse time towards the Earth. The GTO is planar in the Sun-Earth ecliptic plane (x-y in the rotating frame), therefore, an x-y map contains all potential departure locations along the GTO.

Poincaré maps are constructed to generate reference trajectories for initial guesses in a differential corrections scheme. Recall that the $z = 0$ plane is the cross-section to create the Poincaré map. The trajectories along the stable manifold of the quasi-halo orbit are propagated in reverse time and intersections with the $z = 0$ plane are collected as states, $\bar{X}_i^{ST}$; and the states of the departure locations along the GTO are given as $\bar{X}_j^{GTO}$. The number of intersections displayed on the map is condensed by comparing the distance between each position intersection, $\bar{R}_i^{ST}$, and each position on the GTO, $\bar{R}_j^{GTO}$. For example, the distances between a stable manifold state, $\bar{R}_1^{ST}$, and the points on the GTO, $\bar{R}_j^{GTO}$, is computed as $D_j = |\bar{R}_1^{ST} - \bar{R}_j^{GTO}|$ and if $min(D_j) < 2000$ km, then $\bar{X}_1^{ST}$ is displayed on the map in Figure 10. This sampling focuses on intersections that are close to any departure location along the GTO. In Figure 10(a), the GTO departure locations are displayed in white and the stable manifold intersections are in green. This map is created with 75 points

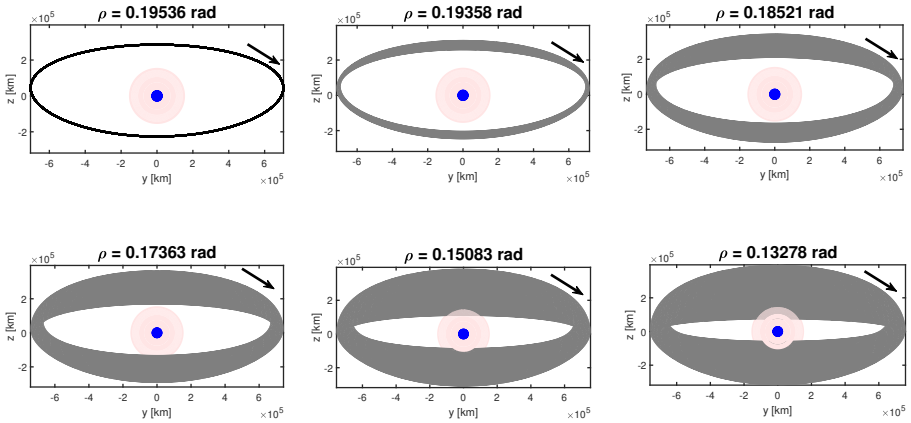

Figure 9: x-z projection of quasi-halo orbits with $C = 3.000802$. The SEZ cone (light red) is measured from the Earth (blue).

around the invariant curve and 100 points along each propagated state in the invariant curve. The x and y position of each stable manifold intersection and departure location along the GTO is plotted in Figure 10 with respect to the Earth. Additionally, the direction of the line associated with a stable manifold point, $\bar{X}_i^{ST}$, or a departure location, $\bar{X}_j^{GTO}$, is computed with the velocity components, $\dot{y}$ and $\dot{z}$, of the respective state. For example, a departure location in white with state $\bar{X}_1^{GTO} = [x_1^{GTO}, y_1^{GTO}, z_1^{GTO}, \dot{x}_1^{GTO}, \dot{y}_1^{GTO}, \dot{z}_1^{GTO}]^T$ is plotted at $(x_1^{GTO} - 1 + \mu, y_1^{GTO})$, recall that the origin is the center of the Earth, and has a line defined with an angle $\beta = \tan^{-1}\left(\frac{\dot{z}_1^{GTO}}{\dot{y}_1^{GTO}}\right)$ measured from $\hat{x}$. After a departure location along the GTO is selected, the ΔV magnitude between the departure location and each stable manifold intersection point in Figure 10(b) is distinguished by color. Potential connections are close in position, but it is also beneficial to match the

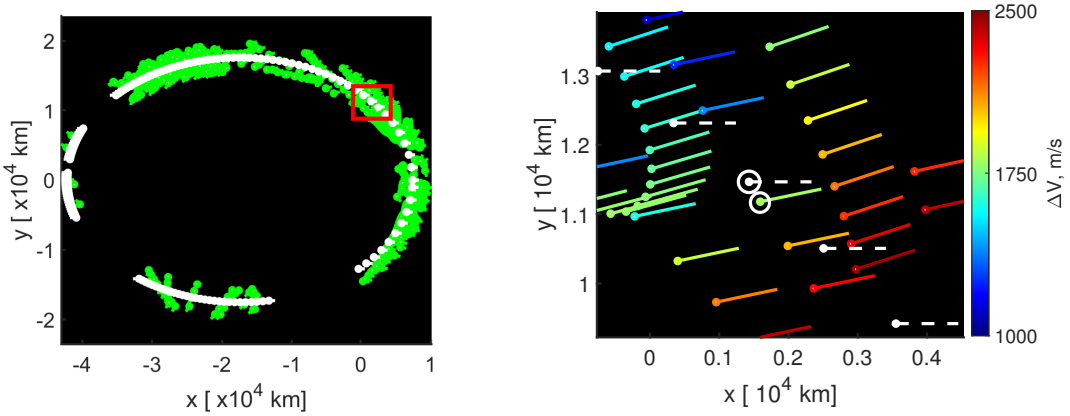

(a) (b)

Figure 10: (a) Poincaré Map for x-y plane. The origin of the map is located at the center of the Earth. (b) Two potential crossings highlighted in white.

velocity directions to avoid large $\Delta V's$ to significantly modify the direction of motion. The transfer links two orbits with different energy values, C, so it is not possible to match all components in the map, i.e., color and velocity direction. The focus is a match in position and the velocity components, $\dot{y}$ and $\dot{z}$, which

implies that a departure from a GTO aligns with a stable manifold trajectory that flows into an L_1 libration point orbit. In Figure 10(b), a potential connection is identified in white at a departure location that is 25.8 min after the perigee along the GTO. In this example, to generate a reference trajectory, ten revolutions along the quasi-halo orbit are stacked along with the GTO arc and the manifold arc. In the corrections scheme, the geometry of the transfer and the quasi-periodic orbit are free to evolve to render a feasible, continuous solution. Therefore, the Jacobi Constant value along the transfer and the quasi-periodic orbit for a corrected solution may be different than the candidate quasi-halo orbit used to generate the map in Figure 10. Energy can be constrained, however, at this preliminary step, allowing C to vary offers flexibility. Projections for the final GTO-to-LPO transfer are plotted in Figure 11. The maneuver is fixed to the location in the Poincaré map and the ΔV magnitude is 1703 m/s. Varying the maneuver location may also lower maneuver magnitude. The transfer does not violate the SEZ during the transfer phase nor in the quasi-periodic orbit.

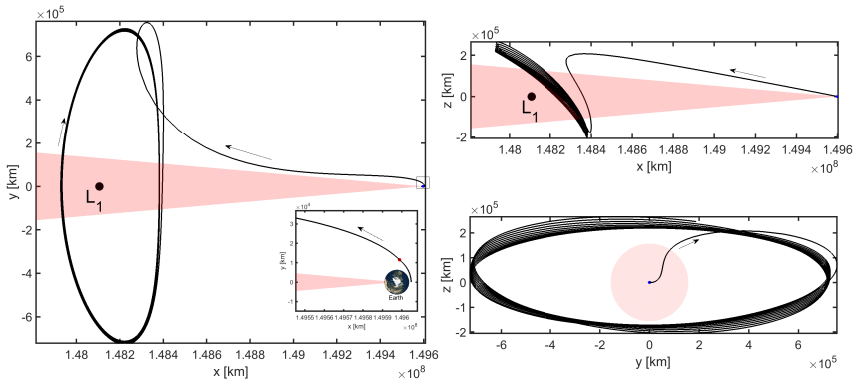

Figure 11: Corrected solution from planar GTO with a departure 25.8 min beyond perigee (in red). The SEV constraint is demonstrated in red.

A comparison between ΔV_{min} and the final ΔV value offers insight concerning the performance of the transfer. For the example in Figure 11, $\Delta V_{min} = 992.9$ m/s and $C = 3.000802$; the difference between the ΔV_{min} and the ΔV in the final solution is large. A maximum ΔV_{max} inequality constraint is enforced during the corrections process to deliver more efficient transfers. The previously converged solution is used as the initial guess for the differential corrector and, incorporating the ΔV_{max} constraint, solutions with low departure ΔV and similar geometry are evaluated. A solution with ΔV_{low} is defined as a solution with low departure ΔV that also maintains the SEZ constraint. A comparison of the shift in the geometry between transfers with a departure location 25.8 min beyond perigee with different ΔV appears in Figure 12. As

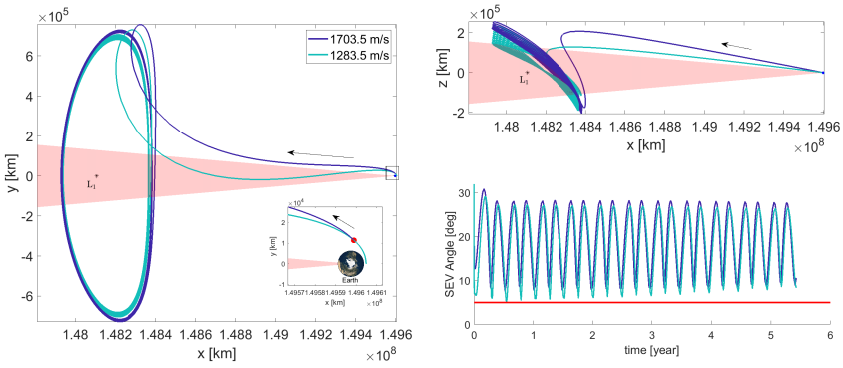

Figure 12: Projections of initial solution (blue) and ΔV_{low} solution (green).

the maximum ΔV magnitude is lowered, the out-of-plane component, Z_B, for the resulting transfer solution

decreases. The ΔV_{low} achieved is 1283.5 m/s while still satisfying the SEZ constraint. Note that this result is not optimized. The solutions in Figure 12 originate from the same departure location along the GTO. The theoretical minimum for the ΔV_{low} maneuver is equal to $\Delta V_{min} = 772.8$ m/s. Note that C is allowed to vary while the departure location beyond perigee is constant during the corrections process. The addition of a ΔV_{max} constraint enables the exploration of transfers from a single departure location.

Exploring the Solution Space

The solution space in the vicinity of a feasible transfer is explored by modifying the orientation of the GTO as well as the departure location. To explore the space, only transfers with ΔV_{low} are examined further. These are transfers with a predetermined orientation and the lowest ΔV magnitude given the previous framework and without crossing into the SEZ. At perigee, the velocity state is defined with the largest magnitude along the GTO, therefore, the transfers that depart from perigee will require a smaller maneuver and share similar characteristics with the ΔV_{low} trajectory in Figure 12. In Figure 13, different trajectories with varying departure locations are compared.

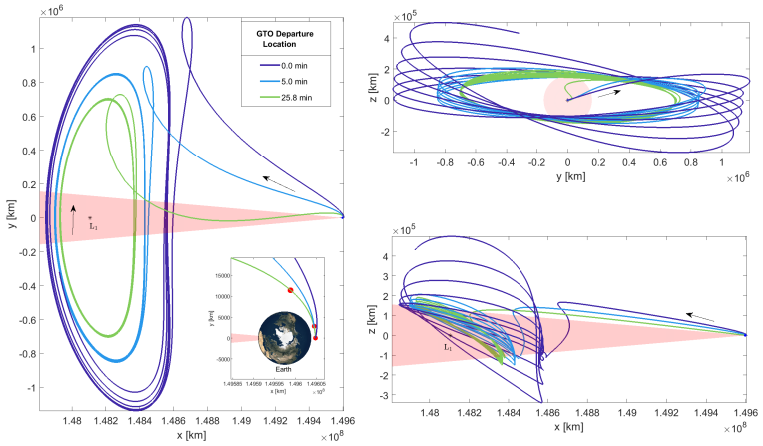

Figure 13: Projections of solutions with varying departure locations after perigee.

From an initial solution with a departure at 25.8 min after perigee, as the departure location approaches the GTO perigee, Y_B and Z_B for the eventual quasi-periodic orbit increase as demonstrated in Figure 13. All the transfer trajectories and the quasi-periodic orbits are constrained to prevent crossing into the SEZ.

The solution space over various orbital inclinations is also explored for departures only from perigee. In this investigation, the orbit inclination is measured relative to the Sun-Earth ecliptic plane in the CRTBP rotating frame. A continuation process with respect to inclination reveals a family of solutions that satisfy the SEZ constraint. The family of transfers is captured in Figure 14. The ΔV_{low} value decreases as inclination increases for departures at perigee and the final quasi-periodic orbit exhibits smaller Z_B values for increasing inclination. Such a result is not unexpected as the constraint limits a minimum Z_B excursion. In this scenario, the

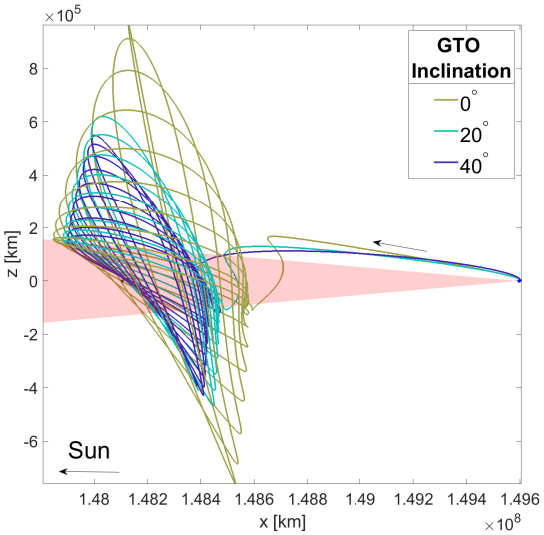

Figure 14: Projection on $x - z$ for solutions from perigee of various inclinations.

orbit inclination is dependent on the requirements for the primary payload via the baseline GTO. While a higher inclination is favorable due to the decreasing values of ΔV_{low}, such would be a constraint placed by the primary payload.

Spacecraft inclination and departure locations are compared for transfers with various values of ΔV_{low}. In Figure 15, the ΔV_{low} value decreases as the departure location moves away from periapsis in a planar GTO. However, this same behavior is not observed for varying inclinations. Various departure locations deliver a range of values for ΔV_{low} given a set of inclinations. Departures near perigee offer low ΔV_{low} magnitudes at higher inclinations, however, this trend varies across departure locations, recall that an optimizer is not employed here. Within the first 50 minutes after perigee, higher inclinations consistently require low ΔV_{low} magnitudes near perigee, but higher magnitudes if departing the GTO beyond 18 minutes post-perigee magnitudes for ΔV_{low} increase. At higher inclinations, the out-of-plane maneuver component is lower for transfers with ΔV_{low} values as apparent in Figure 14 and is not obviously a function of the departure location.

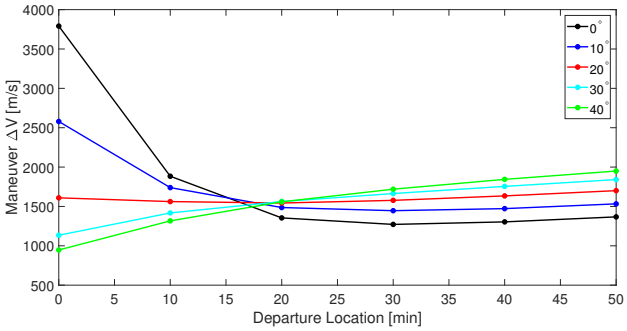

Figure 15: Comparison of departure location measured after perigee and ΔV_{low}.

For convenience, the size of the quasi-periodic orbit is characterized by box dimensions Y_B and Z_B, i.e., functions of the departure location and the inclination of the GTO. An upper bound on the maximum quasi-periodic orbit size in any direction may exist due to attitude constraints on the spacecraft. The exploration of the GTO geometry and the location of departure aids in the search for a feasible solution when size constraints are incorporated. A comparison between quasi-periodic orbits for solutions with a set of inclinations and various departure locations is demonstrated in Figure 16. When the departure point is perigee, then Z_B and Y_B values are smaller at higher inclinations, but this trend is inverted if the departure location shifts to a time beyond perigee.

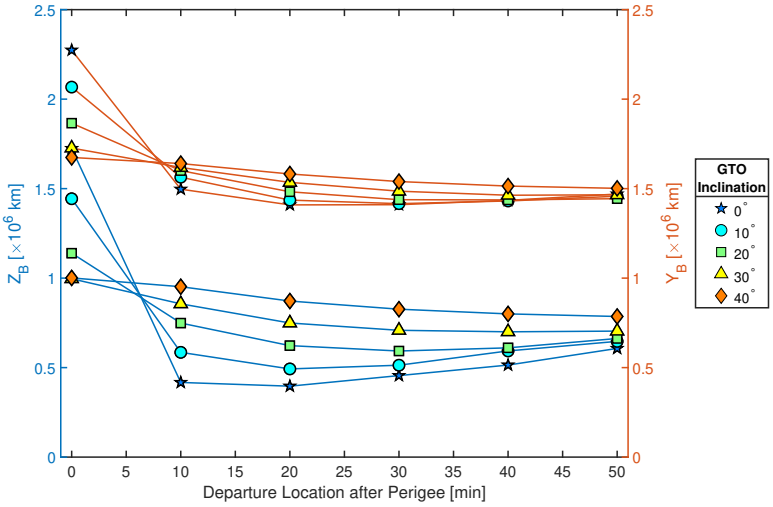

Figure 16: Quasi-periodic orbit size from various inclinations with respect to departure location.

In all sample transfers thus far, the departure GTO is aligned such that the line of apsides is parallel to the rotating x-axis. An analysis based on the precession angle γ is completed for GTOs with different inclinations. Recall that in the CRTBP, the line of apsides shifts counter-clockwise from $\hat{x}$ in the rotating frame by an angle γ measured from the Sun-Earth line. If the departure location is perigee, by evolving through a single revolution on the GTO, the location of the perigee shifts in the rotating frame. A numerical continuation process shifts the γ angle for solutions in Figure 16 that depart at perigee. Recall, that only solutions with ΔV_{low} values are examined. A size comparison for different inclinations is illustrated in Figure 17; recall that Y_B and Z_B are box dimensions that characterize the size of the quasi-periodic orbit. For increasing precession angles, there are increasing values of Y_B and Z_B. Recall that all the solutions explored thus far have been constrained by the SEZ. The maneuver magnitudes, ΔV_{low}, are displayed in Table 1. The magnitude of ΔV_{low} increases as the γ angle increases for inclinations between $20^\circ - 30^\circ$, while ΔV_{low} decreases at 40° inclination. Thus, there appears to be an extremum between 30° and 40° in orientation of the departure GTO.

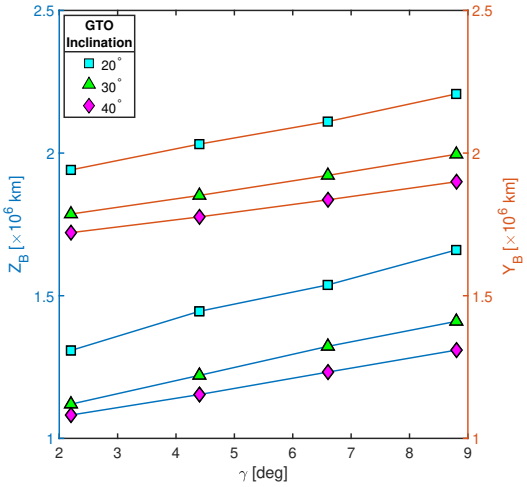

Figure 17: Orbit sizes for solutions with varying γ angle.

Table 1: ΔV_{low} for a set GTO inclinations

20°		30°		40°	
γ (deg)	ΔV_{low} (m/s)	γ (deg)	ΔV_{low} (m/s)	γ (deg)	ΔV_{low} (m/s)
2.200	1625.18	2.200	1134.33	2.201	939.52
4.400	1642.97	4.401	1136.56	4.403	934.90
6.600	1659.86	6.602	1140.23	6.604	931.78
8.800	1677.79	8.802	1144.99	8.806	928.87

An exploration of the solution space through numerical continuation from a feasible trajectory offers insight on a family of solutions with similar characteristics. All transfers and quasi-periodic orbits must satisfy the SEZ constraint; this limits the lowest ΔV that can be achieved for a transfer. Specific GTO orientations, characterized by a combination of inclination, departure location, and precession angle, help to lower the maneuver ΔV.

Transfer from an Inclined GTO

Links involving departure locations along an inclined GTO and stable manifold trajectories associated with quasi-periodic arrival orbits are identified via a new mapping strategy. In a ridesharing scenario, the secondary

payload is restricted to the GTO orientation leveraged by the primary payload. Departure locations along planar GTOs are straightforwardly investigated with an x-y Poincaré map. However, GTOs with non-zero inclinations are not defined in terms of a consistent orbital plane. Therefore, a new mapping approach is implemented to determine connections from locations along inclined GTOs. In this example, the sample planar GTO is rotated to an inclination of 20° with respect to the Sun-Earth ecliptic plane. The trajectories constructed along the stable manifold of a southern quasi-halo orbit, $C = 3.000808$, are leveraged. To identify potential departure locations to link with the manifold trajectories, the propagated states along the GTO are noted and a local region in their vicinity is defined. The scheme, illustrated in Figure 18, demonstrates a set of cylinders that are constructed surrounding the GTO; each cylinder is sized to deliver a feasible link between the GTO and the stable manifold. Recall that a stable manifold intersection is a state $\bar{X}_i^{ST} = [\bar{R}_i^{ST}, \bar{V}_i^{ST}]^T$ and a departure location along a GTO is a state $\bar{X}_j^{GTO} = [\bar{R}^{GTO}(t_j), \bar{V}^{GTO}(t_j)]^T$. The length of the j^{th} cylinder is evaluated as $H_j = \left|\bar{R}^{GTO}(t_{j+1}) - \bar{R}^{GTO}(t_j)\right|$ with GTO positions $\bar{R}^{GTO}(t_j)$ and $\bar{R}^{GTO}(t_{j+1})$. The position of an i^{th} stable manifold intersection along a j^{th} cylinder is defined with p_i^j, the distance along a line from $\bar{R}^{GTO}(t_j)$ to $\bar{R}^{GTO}(t_{j+1})$ for the j^{th} cylinder, and l_i, measured perpendicularly from p_i^j. For example, values of p and l for a stable manifold intersection, $\bar{R}_i^{ST}$, with respect to the first cylinder ($j = 0$), are calculated as,

$$p_i^0 = \frac{\left(\bar{R}^{GTO}(t_1) - \bar{R}^{GTO}(t_0)\right)}{\left|\bar{R}^{GTO}(t_1) - \bar{R}^{GTO}(t_0)\right|} \cdot \bar{R}_i^{ST} \tag{8}$$

$$l_i = \sqrt{\left|\bar{R}_i^{ST} - \bar{R}^{GTO}(t_0)\right|^2 - (p_i^0)^2} \tag{9}$$

The map in Figure 19 demonstrates a series of potential connections at various departure locations along the GTO. Values for distances $P_i^{ST} = p_i^j + \sum_{k=0}^{j-1} H_k$ and $P_j^G = \sum_{k=0}^{j} H_k$ representing an i^{th} stable manifold

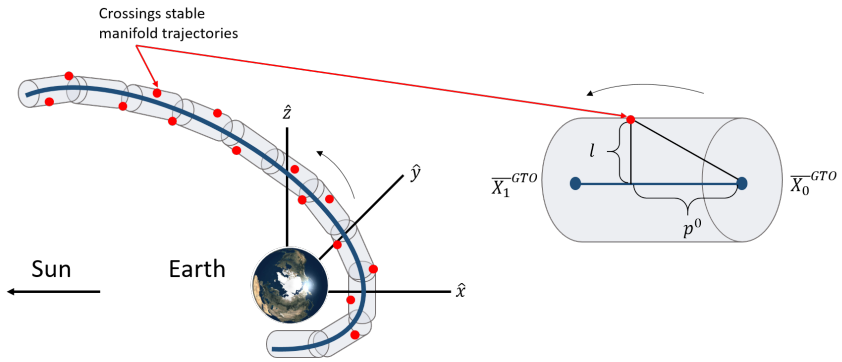

Figure 18: Crossings from various stable manifold trajectories are captured inside cylinders defined with a length p^0 and a constant radius l.

intersections and a GTO departure location in the map, respectively. The map is constructed with cylinders of radius l equal to 500 km and stable manifold intersections lie on the surface of a cylinder, i.e. $l = 500$ km, or lie inside a cylinder, $l < 500$ km. Additionally, a stable manifold intersection may only belong to one cylinder and is constrained by $p_i^j \leq H_j$. Potential near-connections from the stable manifold in Figure 19(a) are depicted in green and the GTO departure locations are in white. Additionally, the direction of the line associated with a stable manifold point, $\bar{X}_i^{ST}$, or a departure location, $\bar{X}_j^{GTO}$, is computed with the velocity components, $\dot{y}$ and $\dot{z}$, of the respective state. For example, a departure location in white with state $\bar{X}^{GTO}(t_1) = [x_1^{GTO}, y_1^{GTO}, z_1^{GTO}, \dot{x}_1^{GTO}, \dot{y}_1^{GTO}, \dot{z}_1^{GTO}]^T$ is plotted at $(P_1^G, l = 0)$ and has a line defined with an angle $\beta = \tan^{-1}\left(\frac{\dot{z}_1^{GTO}}{\dot{y}_1^{GTO}}\right)$ measured from $\hat{x}$. Figure 19(b) illustrates connections with ΔV values, indicated via a range of colors, for the near-connections with respect to the identified deparure location, while the departure locations are given in white. A possible transfer opportunity is identified in Figure 19(b). A reference trajectory is constructed from the near-link highlighted on the map and the arcs are defined in forward time from the GTO and in backwards time along the stable manifold from the pre-specified quasi-halo orbit. The departure location on the GTO is 9.7 min after perigee and the final ΔV_{low} is 1566.7 m/s, as

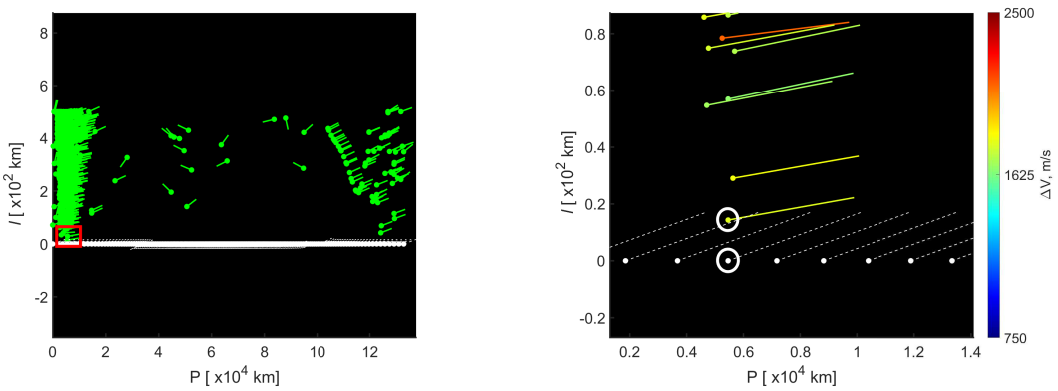

(a) (b)

Figure 19: (a) Map leveraged to identify near crossings into the cylinder created from a GTO. (b) Potential crossings is 14.32 km apart and highlighted in white.

illustrated in Figure 20. The transfer and quasi-periodic orbit also satisfies the SEZ constraint over 5 years. This flexible mapping facilitates the construction of feasible solutions from any departure location along a

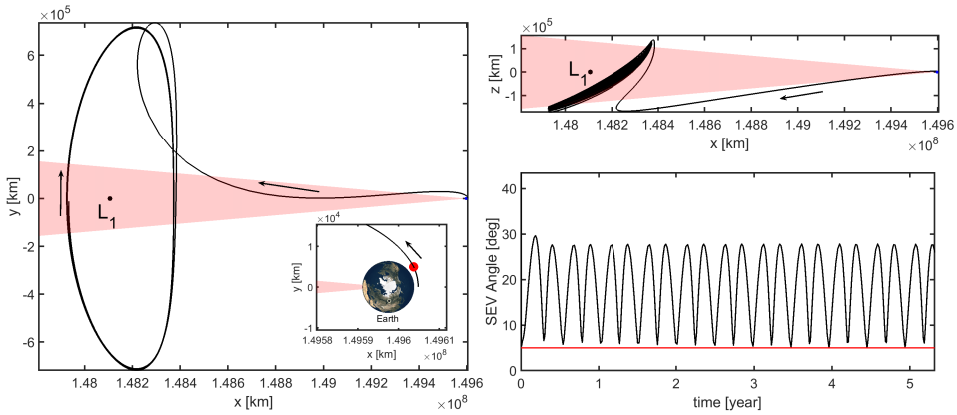

Figure 20: Corrected solution from inclined GTO with a departure 9.7 min after perigee. The ΔV_{low} for this final transfer is 1567 m/s.

GTO with nonzero inclination. Although the mapping is not as intuitive as a Poincaré map with a planar cross-section, it can be applied to expose near-connections from any trajectory.

UNCONSTRAINED TRANSFERS TO QUASI-PERIODIC ORBITS IN L_1 REGION

Unconstrained transfers are produced from feasible transfers that are free to cross into the SEZ cone. Constrained transfers possess high ΔV_{low} values due to the SEZ cone restriction, but solutions with ΔV_{low} values close to the ΔV_{min} magnitudes are identified by omitting the constraint in Equation (6) during the corrections process. A variety of solutions are then constructed without the cone constraint. Constrained solutions are input into the differential corrections process and through a numerical continuation process that decreases the maximum ΔV, a variety of unconstrained solutions are generated. Figure 21 depicts transfers at varying GTO inclinations with departure locations at perigee. A comparison between inclination of the given departure GTO and the size of the quasi-periodic orbit is plotted in Figure 22 and values of ΔV_{low} are displayed in Table 2. For unconstrained transfers and orbits, both Y_B and Z_B values increase as the inclination increases. The trend in Figure 22 supports the intuition that more efficient transfers from planar

GTOs will also be planar. Additionally, as the inclination of the GTO increases, the out-of-plane component

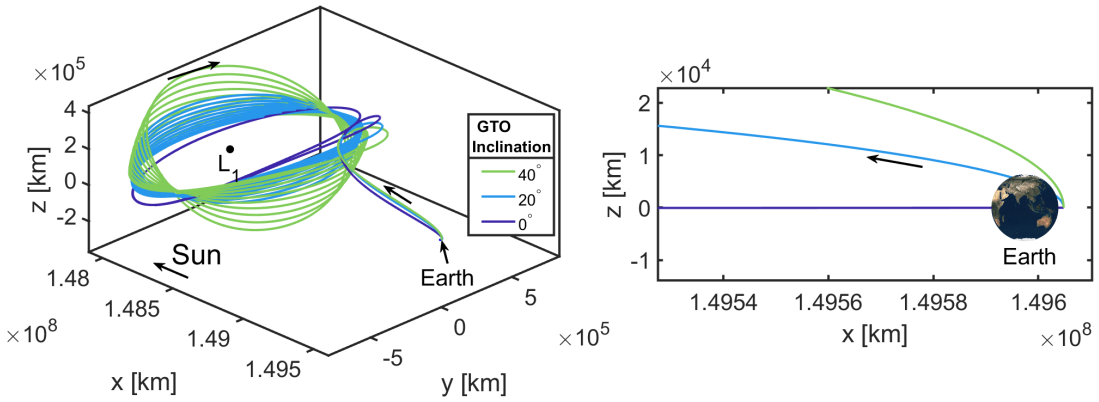

Figure 21: Unconstrained solution geometry at different inclinations. The out-of-plane component of the quasi-periodic orbit increase with inclination.

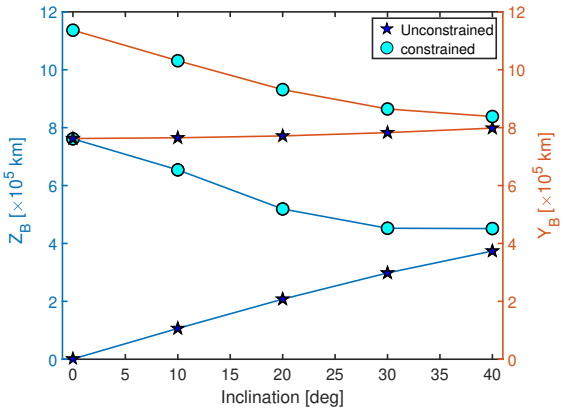

Figure 22: Orbit size for unconstrained and constrained transfers

Inclination (deg)	ΔV_{low} (m/s)	ΔV_{min} (m/s)
0	773.44	773.23
10	773.26	773.24
20	773.28	773.27
30	773.33	773.32
40	773.38	773.28

Table 2: ΔV for unconstrained transfers

of the transfer and the quasi-periodic orbit also increases; recall this is measured by box dimension, Z_B. Note that the orbit size trend in Figure 22 is opposite of the constrained transfers, which must be outside the SEZ cone. In Table 2, ΔV_{low} values are close to the ΔV_{min} magnitudes corresponding to each transfer, note that these solutions have not been optimized.

By omitting the SEZ cone constraint, more efficient transfers to the Sun-Earth L_1 vicinity are generated with varying geometry. Previously constrained transfers are numerically continued to construct these efficient transfers from any departure location along the GTO. As expected, the size of the solution is dependent on the inclination of the GTO. However, in a ride-share scenario, the GTO inclination is determined by the primary payload; the secondary payload is subject to certain communications constraints.

CONCLUDING REMARKS

Quasi-periodic orbits possess dynamical structures that are leveraged to construct transfers from Geosynchronous Transfer Orbits towards orbits near Sun-Earth L_1. Using numerical techniques, a family of quasi-halo orbits is generated from periodic Sun-Earth halo orbits. For a ridesharing scenario, flexible and efficient direct transfers are generated to quasi-periodic orbits near L_1 from secondary payloads along a GTO. The effects of varying orbit inclination, orientation, and departure location on the quasi-periodic size are investigated. For transfers using a Solar Exclusion Zone cone constraint, ΔV values decrease, as expected, when departing at GTO perigee with increasing inclination. However, this trend is not necessarily true when departing at different locations along a GTO. Additionally, the size of the quasi-periodic orbit, expressed using box dimension values, follows a similar trend to the ΔV values. At higher inclinations, dimensions Z_B and Y_B decrease when departing at GTO perigee, but this trend is inverted when departing along different locations along the GTO. By omitting the cone constraint, more efficient transfers are generated with lower ΔV values and smaller Z_B and Y_B dimensions. Note that all transfers generated were not optimized. A combination of increasing inclination and shifting the departure location near GTO periapsis aids in more efficient ΔV magnitudes.

ACKNOWLEDGMENT

The authors thank Mr. Michael Mesarch for introducing this research topic. Assistance and guidance from colleagues in the Multi-Body Dynamics Research group at Purdue University is much appreciated as is the support of the Purdue University School of Aeronautics and Astronautics including access to the Rune and Barbara Eliasen Visualization Laboratory. This material is based upon work supported by the National Science Foundation Graduate Research Fellowship Program under Grant No. DGE-1333468. Any opinions, findings, and conclusions or recommendations expressed in this material are those of the author(s) and do not necessarily reflect the views of the National Science Foundation.

REFERENCES

[1] P. Tompkins, R. Hunt, M. D'Ortenzio, K. Galal, D. Foreman, J. Munger, M. Shirley, J. Strong, R. Barber, and E. Drucker, "Flight operations for the LCROSS lunar impactor mission," *SpaceOps 2010 Conference Delivering on the Dream Hosted by NASA Marshall Space Flight Center and Organized by AIAA*, 2010, p. 1986.

[2] M. Stender, C. Pearson, J. Maly, and C. Loghry, "Mission case studies using the rideshare enabling Orbital Maneuvering Vehicle," *2015 IEEE Aerospace Conference*, IEEE, 2015, pp. 1–9.

[3] R. Farquhar, "The flight of ISEE-3/ICE-Origins, mission history, and a legacy," *AIAA/AAS Astrodynamics Specialist Conference and Exhibit*, 1998, p. 4464.

[4] C. Roberts, "Long term missions at the Sun-Earth libration point L1: Ace, SOHO, and WIND," *Advances in the Astronautical Sciences*, Vol. 142, 01 2012, pp. 1263–1282.

[5] D. W. Dunham, S. Jen, C. Roberts, A. Seacord, P. Sharer, D. Folta, and D. Muhonen, "Transfer trajectory design for the SOHO libration-point mission," *Washington, DC International Astronautical Federation Congress*, 1992.

[6] H. Franz, P. Sharer, K. Ogilvie, and M. Desch, "WIND nominal mission performance and extended mission design," *AIAA/AAS Astrodynamics Specialist Conference and Exhibit*, 1998, p. 4467.

[7] H. Franz, "A Wind Trajectory Design Incorporating Multiple Transfers Between Libration Points," *AIAA/AAS Astrodynamics Specialist Conference and Exhibit*, 2002, p. 4525.

[8] M. Lo, B. Williams, W. Bollman, D. Han, Y. Hahn, J. Bell, E. Hirst, R. Corwin, P. Hong, and K. Howell, "Genesis mission design," *AIAA/AAS Astrodynamics Specialist Conference and Exhibit*, 1998, p. 4468.

[9] J. Burt and B. Smith, "Deep space climate observatory: The DSCOVR mission," *2012 IEEE Aerospace Conference*, IEEE, 2012, pp. 1–13.

[10] C. Roberts, S. Case, J. Reagoso, and C. Webster, "Early Mission Maneuver Operations for the Deep Space Climate Observatory Sun-Earth L1 Libration Point Mission," 2015.

[11] N. Bosanac, C. M. Webster, K. C. Howell, and D. C. Folta, "Trajectory Design and Station-Keeping Analysis for the Wide Field Infrared Survey Telescope Mission," *AAS/AIAA Astrodynamics Specialist Conference*, 2017.

[12] G. Gómez, A. Jorba, J. Masdemont, and C. Simó, "Study of the transfer from the Earth to a halo orbit around the equilibrium pointL 1," *Celestial Mechanics and Dynamical Astronomy*, Vol. 56, No. 4, 1993, pp. 541–562.

[13] Z. P. Olikara, *Computation of quasi-periodic tori and heteroclinic connections in astrodynamics using collocation techniques*. Ph.D. Dissertation, University of Colorado Boulder, 2016.

[14] G. Gómez, J. Masdemont, and C. Simó, "Quasihalo orbits associated with libration points," *Journal of the Astronautical Sciences*, Vol. 46, No. 2, 1998, pp. 135–176.

[15] K. C. Howell and H. J. Pernicka, "Numerical determination of Lissajous trajectories in the restricted three-body problem," *Celestial Mechanics*, Vol. 41, No. 1-4, 1987, pp. 107–124.

[16] B. P. McCarthy and K. C. Howell, "Trajectory Design Using Quasi-Periodic Orbits in the Multi-Body Problem," *29th AAS/AIAA Space Flight Mechanics Meeting, Hawaii, USA*, 2019.

[17] D. Scheeres, S. Van wal, Z. Olikara, N. Baresi, *et al.*, "Dynamics in the Phobos environment," *Advances in Space Research*, Vol. 63, No. 1, 2019, pp. 476–495.

[18] N. Baresi, *Spacecraft Formation Flight on Quasi-periodic Invariant Tori*. Ph.D. Dissertation, University of Colorado Boulder, 2017.

[19] N. Bosanac, *Exploring the influence of a three-body interaction added to the gravitational potential function in the circular restricted three-body problem: a numerical frequency analysis*. MS Thesis, Purdue University, 2012.

[20] V. Szebehely, "Theory of orbits: the restricted problem of three bodies," tech. rep., Yale univ New Haven, Connecticut, 1967.

[21] W. Schlei, K. C. Howell, X. Tricoche, and C. Garth, "Enhanced visualization and autonomous extraction of Poincare map topology," *The Journal of the Astronautical Sciences*, Vol. 61, No. 2, 2014, pp. 170–197.

[22] W. S. Koon, M. W. Lo, J. E. Marsden, and S. D. Ross, *Dynamical Systems, the Three Body Problem and Space Mission Design*. Springer-Verlag New York Incorporated, 2006.

[23] G. Gómez and J. M. Mondelo, "The dynamics around the collinear equilibrium points of the RTBP," *Physica D: Nonlinear Phenomena*, Vol. 157, No. 4, 2001, pp. 283–321.

[24] Z. P. Olikara and D. J. Scheeres, "Numerical method for computing quasi-periodic orbits and their stability in the restricted three-body problem," *Advances in the Astronautical Sciences*, Vol. 145, No. 911-930, 2012.

[25] D. Guzzetti, N. Bosanac, A. Haapala, K. C. Howell, and D. C. Folta, "Rapid trajectory design in the Earth–Moon ephemeris system via an interactive catalog of periodic and quasi-periodic orbits," *Acta Astronautica*, Vol. 126, 2016, pp. 439–455.

[26] M. Kakoi, *Design of Transfers from Earth-Moon L1/L2 Libration Point Orbits to a Destination Object*. Ph.D. Dissertation, Purdue University, 2015.

[27] T. A. Pavlak and K. C. Howell, "Evolution of the out-of-plane amplitude for quasi-periodic trajectories in the Earth–Moon system," *Acta Astronautica*, Vol. 81, No. 2, 2012, pp. 456–465.